This article has been accepted for publication in a future issue of this journal, but has not been fully edited. Content may change prior to final publication. Citation information: DOI 10.1109/TNANO.2015.2494019, IEEE Transactions on Nanotechnology

A Trace and Retrace Scanning Combined Topography Reconstruction Strategy for Fast Scanning Atomic Force Microscopies

Xiao Ren, Yongchun Fang, *Senior Member, IEEE,* and Yinan Wu

***Abstract*—For nearly all atomic force microscopies (AFMs) utilized now, only the signals in trace scanning process are employed to reconstruct the sample surface topography, while the data of retrace scanning process is just used for adjustment. In this paper, a novel trace and retrace scanning combined (TRSC) topography reconstruction strategy, which successfully utilizes data from both trace and retrace processes, is proposed for AFMs to increase surface reconstruction accuracy. Specifically, two reconstructed topography images are obtained, one is for trace scanning and the other is for retrace scanning; the hysteresis distortion is successfully compensated with a data fusion based post-processing method; the alignment for trace and retrace images is further guaranteed with a feature point based strategy; then the two images are combined together with confidence levels to reconstruct the final accurate topography image. Compared with conventional scanning method, the proposed TRSC imaging algorithm provides much more accurate image for the sample surface, and it is especially valid for high-speed scanning tasks. Some simulation and experimental results are included to demonstrate the superior performance of the proposed imaging method.**

***Index Terms*—Atomic Force Microscopy (AFM), Combined Imaging Method, Hysteresis Compensation, Fast Scanning.**

I. Introduction

SINCE its invention, atomic force microscopy (AFM) [1] has brought a great revolution in the domain of nano-science and nano-technology [2], [3]. Attributed to its outstanding advantages such as high resolution [4] and great convenience for sample preparation, AFM has been widely used in life science, material engineering [5], etc.

For AFM systems, the main bottleneck for further application is the comparatively low scanning speed, as it usually takes several minutes to yield a high-quality image. Yet, to supervise some chemical or biological processes on-line, much higher speed is required without sacrificing imaging resolution. After analyzing the properties of an AFM system, it is known that the scanning speed is mainly limited by the dynamic characteristics of Z-axis sub-system. That is, to obtain a trusty image for a sample, the tip of an AFM scans through the sample surface and it needs to stay long enough at each point to collect steady-state data for topography construction. Based on this observation, some researchers have taken various efforts to shorten the response time of an AFM to implement higher speed scanning tasks, which can be mainly classified into two categories of high-performance hardware adoption, and more advanced control/imaging algorithms development.

So far, many results have been reported on designing some elaborate scanner structures [6], [7], [8], [9], or utilizing a piezo-scanner with high resonant frequency to enhance the bandwidth of the vertical sub-system. For example, in [10], a dual actuated Z-axes sub-system is proposed to significantly increase the closed-loop bandwidth by combining a long-range, low-bandwidth actuator with a short-range, high-bandwidth actuator. A flexure-based nanopositioner with parallel-kinematic configurations is well designed in [11], which has high resonant frequencies along all X-, Y-, Z-axes. In [12], a fast Z-scanner consisting of a piezoelectric stack actuator and a diaphragm flexure is presented to implement fast scanning. It is straightforward to see that the work on the hardware improvement presents some unavoidable drawbacks, such as additional cost, inconvenient combination with the existing software, etc., which then prevents the further applications on AFMs. Compared with the work on hardware reform, more efforts have been put on designing advanced control/imaging strategies to enable an AFM to scan samples with sufficiently high speed. An output feedback robust adaptive controller is designed for Z-axis tracking control in [13] with the consideration of output saturation problem for tapping mode; and an observer-based MPC-notch controller is proposed in [14] to implement fast scanning by improving the damping of the resonant mode of the AFM piezoelectric tube; in [15], a practical dynamic imaging method with the consideration for the dynamic characteristics of piezo-scanner is well designed, and some other advanced control/imaging methods are presented in [16], [17], [18], [19], [20]. Unfortunately, most of the proposed advanced strategies are too complicated to be implemented in real AFM apparatus; besides, although some of the proposed methods illustrate good performance on specific aspects, it is hard to combine different methods together to get further improvements.

When an AFM is employed to scan a sample, the tip usually follows some pre-set raster fashion trajectories to obtain data to image the sample. Unfortunately, for currently prevailing methods, only the date obtained from the trace trajectory is utilized to construct the surface topography of the sample, while the data from retrace process is just utilized for adjustment. It is not difficult to see that the retrace process also provides use-

This work was supported by National Natural Science Foundation of China (61127006, 61325017).

All the authors are with the Institute of Robotics and Automatic Information System, Nankai University, Tianjin, China, and Tianjin Key Laboratory of Intelligent Robotics, Tianjin, China (email: fangyc@nankai.edu.cn).

This article has been accepted for publication in a future issue of this journal, but has not been fully edited. Content may change prior to final publication. Citation information: DOI 10.1109/TNANO.2015.2494019, IEEE Transactions on Nanotechnology

ful information for surface construction. Specifically, for the scanning points where the retrace scanning process achieves better control effect than trace process, more accurate topography image can be constructed from retrace process data. Based on this idea, a novel Trace and Retrace Scanning Combined (TRSC) bilateral topography reconstruction strategy, which fully utilizes data from both trace and retrace processes, is designed for AFMs to enhance imaging performance. The proposed TRSC bilateral strategy includes three main steps of hysteresis compensation, trace and retrace images alignment, and bilateral combination imaging. Compared with currently existing methods, the proposed method presents the following advantages: i. it involves no hardware replacement; ii. it provides more accurate topography reconstruction, especially for sufficiently high scanning tasks; iii. it can be easily combined with other hardware/software imaging methods, and can be conveniently adopted in existing AFM systems.

The remainder of this paper is organized as follows. In Section II, the basic idea and general scheme for this novel imaging method is stated. Subsequently, the TRSC topography reconstruction strategy is introduced in detail in Section III. Followed are some simulation and experimental results in Section IV to demonstrate the performance of the imaging method. Section V provides the conclusion of the paper.

II. Basic Idea and General Scheme

For most commonly used AFM systems, the scanner is controlled to track a raster fashion trajectory along the sample surface (in the X-axis), while the sub-system in Z-axis is controlled to keep the separation between the surface and the micro-cantilever tip constant and the control signal/error is employed to extract topography information for the sample. To ensure satisfactory imaging performance, it is required that the system reach steady-state for each scanning point. When scanning at low speed, it is not difficult to meet this requirement and the trace scanning signal (in Z-axis) can be utilized to construct a reliable image for the sample, provided that the signal is not contaminated by measurement noise. However, for fast scanning tasks, this practice cannot provide satisfactory result because of the following reasons: on one hand, as the tip stays in each scanning point shortly, it cannot be stabilized for the steep points due to the inherent dynamic property of the scanner, hence, only transient signals, instead of steady-state ones, can be obtained and then utilized to calculate the undulation of those points. On the other hand, when the scanning speed is sufficiently high, the measurement is apt to be contaminated by various noise. To attack these problems, the so-called TRSC bilateral topography reconstruction strategy, which not only employs trace scanning signals to calculate the sample surface topography, but also utilizes retrace signals as remedial measurement, is designed to enhance imaging performance.

To better describe the TRSC bilateral imaging strategy, we utilize the following example of scanning a calibration grating to illustrate the general idea of the strategy. When the trace and retrace scanning results are well consistent with each other, the illustrative sketch of one-line results for the calibration grating is presented in Fig. 1, where Fig. 1 (a) and (b) respectively show the topography and the control error for trace scanning process, while Fig. 1 (c) and (d) plot the results for retrace scanning. As can be seen from the figure, in segment AB, the control error for trace scanning process is much larger than that of the retrace scanning process. Then, in this segment, the calculated result from retrace scanning is much more reliable than that from trace scanning. Similarly, it can be seen from the figure that trace scanning provides better topography construction result for segment CD.

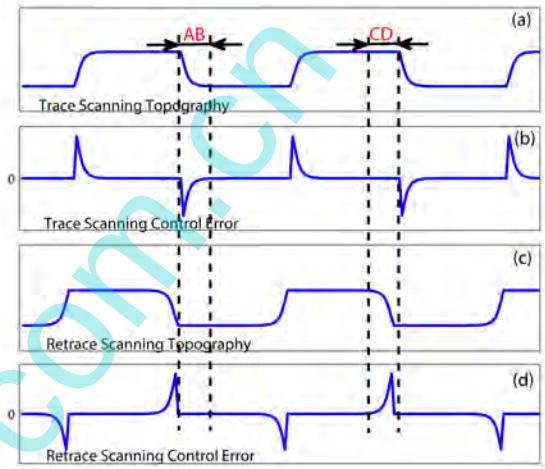

Fig. 1. One-line scanning sketch graph: (a) trace scanning topography, (b) trace scanning control error, (c) retrace scanning topography, (d) retrace scanning control error. For segment AB, retrace topography performs better than the trace one, while the trace topography shows better for segment CD.

Based on the previous description, we know that if utilizing data from both trace and retrace processes, along with the corresponding control error, more accurate topography image can be obtained for the scanned sample. Therefore, we propose the TRSC bilateral strategy, which consists of the following three steps of distortion compensation, alignment and bilateral imaging to construct a satisfactory image for the sample. Specifically, the first step aims to compensate the distortion caused by the nonlinear characteristics of the scanner, including hysteresis, creep, vibration, etc., with hysteresis being the most important one, so as to make the trace and retrace scanning images be consistent with each other. Based on the results of the first step, the second step tries to align the bilateral images by extracting features from both images and then employ some nonlinear technique to further remove the influence of the unaddressed nonlinearities such as creep and vibration. Subsequently, the third step fuses the data from both directions to construct a reliable image for the sample surface.

AFM imaging process can be divided into two parts: Z-axis tracking subprocess and topography reconstruction subprocess. This paper mainly deals with the second subprocess of how to utilize the obtained tracking data (e.g., control voltages, control errors) to reconstruct the topography. It is rational to find out that the proposed TRSC imaging method can be conveniently combined with some advanced tracking strategies,

This article has been accepted for publication in a future issue of this journal, but has not been fully edited. Content may change prior to final publication. Citation information: DOI 10.1109/TNANO.2015.2494019, IEEE Transactions on Nanotechnology

such as [21], [22], to further increase its performance.

III. TRSC Topography Reconstruction Strategy Design

A. Data Fusion Based Hysteresis Compensation

Hysteresis compensation is one of the research hot topics for piezo-scanner. Current control-based methods can be classified as feedback control [23], [24], [25], [26], [27] and feedforward control [28], [29], [30]. These methods provide effective compensation for the hysteresis distortion; however, due to the limitation of control bandwidth in feedback loop and the inaccuracy of the reverse model of piezo-scanner, these methods cannot achieve satisfactory performance for fast scanning tasks. In the TRSC bilateral imaging strategy, to obtain accurate topography images free of hysteresis distortion, a data fusion based post-processing method is proposed for hysteresis compensation, wherein the hysteresis characters are measured in advance, and the topography height values are then calculated from the original distorted topography image. For the sake of brevity, the case of X direction is selected as an illustrative example to describe the hysteresis compensation strategy, yet the discussion is also valid for the other directions.

Usually the control signal for the piezo-scanner is chosen as triangular waves. If the Hysteresis is perfectly compensated, the points, denoted as the expected points in Fig. 2(a), will distribute evenly along a line, based on which a trusty image can then be reconstructed for a sample. Otherwise, the tracking points will be unevenly distributed, as shown in Fig. 2(b) for trace scanning and Fig. 2(c) for retrace scanning, which then brings inaccuracy for the reconstructed images. Therefore, we need to set up the relationship between the expected points and the real tracking points to effectively compensate the hysteresis.

To implement the compensation, the hysteresis characters (hysteresis circles) are measured in advance with high-bandwidth position sensors in several considered frequencies such as 5Hz, 10Hz, 20Hz, 50Hz, etc. The noise of sensor is addressed by averaging for large repeated measurements. Then the maximum displacement of piezo-scanner in X-axis, denoted as $s_{\max}$, is equally divided into N parts, with N being the resolution for the reconstructed topography image. The N expected points are noted as s_1, s_2, ..., s_q, ..., s_N, as shown in Fig. 2. For the point s_q, we can find the nearby trace tracking points ttp_k, ttp_{k+1}, etc., where ttp_k stands for the k-th trace tracking point. In the same way, the retrace tracking points near s_q can be obtained. As the situations are similar, only the compensation for trace scanning topography is described here.

The topography height value for the trace tracking points can be calculated by some specific imaging algorithms [15], [19]. Then the topography height for the expected point s_q, denoted as h_q, can be calculated as:

$$h_q = \sum_{i \in \Omega_1} \alpha_i h_i \tag{1}$$

where Ω_1 is the neighboring point set consisting of trace tracking points near s_q, h_i is the height signal for the i-th trace tracking point in Ω_1, and α_i is the weight coefficient satisfying:

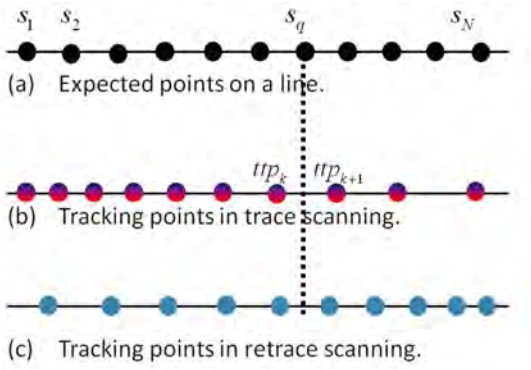

Fig. 2. Expected points in one line for topography reconstruction, and the corresponding tracking points in trace scanning and retrace scanning.

$$\sum_{i \in \Omega_1} \alpha_i = 1 \tag{2}$$

Now the task is to determine the neighboring point set Ω_1 and the weight coefficient α_i.

For the studied AFM system, the neighboring point set Ω_1 is chosen as several points near s_q on the same line. Specifically, for the experimental results presented subsequently, if s_q is between two trace tracking points ttp_k and ttp_{k+1}, these points ttp_k and ttp_{k+1} are chosen as Ω_1; if s_q is exactly located on one trace tracking point ttp_k, then ttp_{k-1}, ttp_k, and ttp_{k+1} are chosen as Ω_1.

The weight coefficient α_i, corresponding to the trace tracking point ttp_i, is a synthesis of its control error e_i in Z-axis, and the distance between the point ttp_i and the expected s_q, which is explicitly defined as:

$$\alpha_i = \frac{\lambda_i \beta_i}{\sum_{j \in \Omega_1} \lambda_j \beta_j} \tag{3}$$

where λ_i is the confidence level value for the topography height of ttp_i, and β_j is the forgetting factor, which are respectively defined as:

$$\lambda_i = \exp\left(\frac{-|e_i|}{3\sigma}\right) \tag{4}$$

with σ being the standard deviation of all the control errors in Z-axis, and

$$\beta_j = \frac{1}{\theta_1 + \left(\frac{dis(ttp_j, s_q)}{\Delta s}\right)^2} \tag{5}$$

with Δs standing for the distance between two adjacent expected points such as s_q and s_{q-1}, $dis(ttp_j, s_q)$ being the distance between the point ttp_j and s_q, and θ_1 representing a small positive constant introduced to avoid singularity, specifically chosen as 0.1 in the subsequent experiments.

This article has been accepted for publication in a future issue of this journal, but has not been fully edited. Content may change prior to final publication. Citation information: DOI 10.1109/TNANO.2015.2494019, IEEE Transactions on Nanotechnology

Therefore, a compensated topography image can be obtained from Equation (1). With high bandwidth and high accuracy position sensors, the hysteresis characters of the piezo-scanner can be well measured, based on which the hysteresis distortion can be effectively compensated by utilizing (1).

With the aforementioned compensation method, two new topography images can be obtained, one for trace scanning and the other for retrace scanning. Preparing for the following steps, the newly control error images are calculated as:

$$e_q = \sum_{i \in \Omega_1} \alpha_i e_i \tag{6}$$

where e_q is the Z-axis control error at point s_q. This equation is similar with Equation (1).

After the compensation, the trace and retrace topography images are roughly consistent with each other.

Remark 1: Control-based hysteresis compensation is to utilize the control signal to make the piezo-scanner go along a straight line, which is usually based on a very complex dynamic model for the piezo-scanner. Comparatively, the proposed data fusion based compensation method actually utilizes hysteresis distorted images to calculate the expected points, so as to reconstruct a more reliable image, which requires no dynamic model and can be implemented without much difficulty.

Remark 2: To implement the proposed hysteresis compensation strategy, one high-quality capacitive displacement sensor is utilized to initially calibrate the hysteresis circle (horizontal positions) in several considered frequencies (e.g. 1Hz, 10Hz, 50Hz, etc.) and overall displacements (e.g. $1\mu m$, $10\mu m$, $20\mu m$, etc.). With the position calibration sets, the neighboring point sets with respect to each expected point can be conveniently obtained.

B. Feature Point Based Alignment

To further align the trace and retrace topography/error images, a feature point based alignment algorithm is proposed here. Specifically, some feature point candidates from trace/retrace images are extracted first, based on which some feature point-pairs can be then obtained, which are subsequently utilized to align the retrace images with the trace ones.

1) Definition and Extraction for Feature Point Candidates: In the scanning area, the topography may fluctuate sharply at some points; therefore, the error images will show great deviations at these points. After some analysis, feature-point candidates are chosen as those points where the error is beginning to increase sharply, since this feature appears in both trace and retrace error images and these points are usually consistent in the two images.

Specifically, feature point candidates sets are defined as the following sets, denoted as Ω_t and Ω_r for trace and retrace images respectively:

$$\Omega_t := \left\{ \begin{array}{l} (i,j) \,|\exists k_1 > j,\ E_t(i,k_1) > ub \\ and\ \ \forall k_2,\ j < k_2 < k_1,\ E_t(i,k_2) > lb \end{array} \right\} \tag{7}$$

$$\Omega_r := \left\{ \begin{array}{l} (i,j) \,|\exists k_1 < j,\ E_r(i,k_1) > ub \\ and\ \ \forall k_2,\ k_1 < k_2 < j,\ E_r(i,k_2) > lb \end{array} \right\} \tag{8}$$

where ub and lb are two threshold values. $E_t(i,j)$ is the control error in trace scanning image at point (i,j); similarly, $E_r(i,j)$ is the error of retrace scanning.

Equation (7) shows that, the point (i,j) in trace scanning image is selected as a feature point candidate only if it satisfies the following two conditions:

i. There is one point (i,k_1) right to (i,j) on the same row, whose control error is larger than ub.

ii. From point (i,k_1) to the left, (i,j) is the first point whose control error is lower than lb.

Equation (8) applies the same requirements.

To better show the clarification, the experimental results of one-line first-step compensated error curves are ploted in Fig. 3, where the red dashed line is for trace scanning, and the blue solid line is for retrace scanning, while the bold black points are the extracted feature point candidates from Equation (7) and Equation (8). Good pair characteristics can be clearly seen from Fig. 3, which plays the pivotal role for the subsequent alignment.

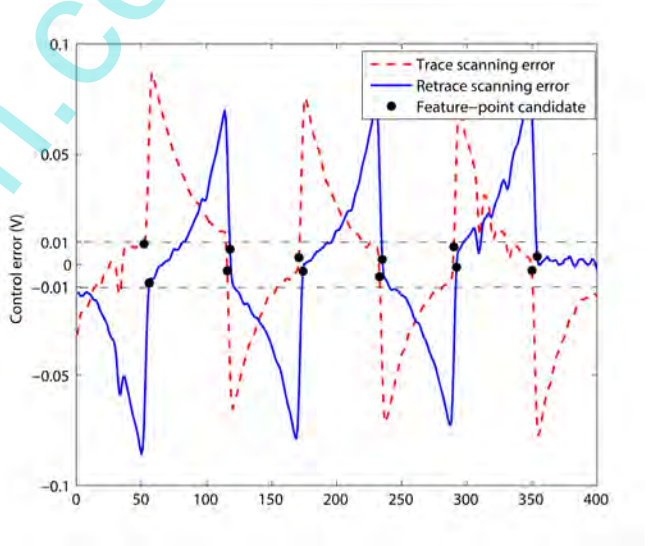

Fig. 3. Feature-point candidates extraction. The feature-point candidates are chosen as the points where the error is beginning to increase sharply.

2) Definition and Extraction for Feature Point-Pairs: The feature point-pairs are defined as a set consisting of the points from Ω_t and Ω_r, which are sufficiently close to each other:

$$\Omega_{fpp} := \left\{ \begin{array}{l} (m,n) \,|\exists r,\ (r,m) \in \Omega_t,\ and\ (r,n) \in \Omega_r, \\ and\ \ |m-n| < w \end{array} \right\} \tag{9}$$

where w is the predicted threshold value, empirically chosen as a small positive integer, it can effectively deal with the induced noise.

The definition implies that, in one line, if two feature point candidates, one from trace scanning and the other from retrace scanning, are sufficiently close to each other, they will be regarded as a feature point-pair.

This article has been accepted for publication in a future issue of this journal, but has not been fully edited. Content may change prior to final publication. Citation information: DOI 10.1109/TNANO.2015.2494019, IEEE Transactions on Nanotechnology

3) Images Alignment: Draw all the feature point-pairs on a plane, a least square polynomial curve is then fitted to present the transform between the trace and retrace scanning images. Based on this relationship, a retrace image can then be conveniently mapped, so that it can be well aligned with the corresponding trace image. Notice that, during the mapping process, only the retrace images have been mapped, while the trace ones are kept invariant.

By now, the trace and retrace topography/error images are well consistent with each other, which provides the foundation for the subsequent combination imaging.

C. The Combination Strategy

After the alignment operation, the topography and control error images for trace scanning are denoted as I_t and E_t respectively. For retrace scanning, the images are represented as I_r and E_r. The final calculated topography image is recorded as I_{final}. The notation $I_t(i,j)$ stands for the value at the point (i,j) in image I_t, the notations of $I_r(i,j)$, $E_t(i,j)$, $E_r(i,j)$, and $I_{final}(i,j)$ have similar implication.

To deal with measurement noise, when calculating the value $I_{final}(i,j)$, the points around (i,j) in I_t and I_r are utilized to yield more reliable results:

$$I_{final}(i,j) = \sum_{(p,q)\in\Omega_2} I_t(p,q)\,\gamma_t(p,q) + \sum_{(p,q)\in\Omega_2} I_r(p,q)\,\gamma_r(p,q) \tag{10}$$

where Ω_2 is the neighboring point set around point (i,j), $\gamma_t(p,q)$ is the yet-to-determine weight coefficient at point (p,q) for trace scanning and $\gamma_r(p,q)$ is similarly defined for retrace scanning. The weight coefficients satisfy the following constraint:

$$\sum_{(p,q)\in\Omega_2} \gamma_t(p,q) + \sum_{(p,q)\in\Omega_2} \gamma_r(p,q) = 1 \tag{11}$$

To calculate the weight coefficients, we first define the confidence level values for the point (i,j) in the topography images I_t and I_r, respectively denoted as $\eta_t(i,j)$ and $\eta_r(i,j)$, in the following manner:

$$\eta_t(i,j) = \exp\left(\frac{-|E_t(i,j)|}{3\sigma_t}\right) \tag{12}$$

$$\eta_r(i,j) = \exp\left(\frac{-|E_r(i,j)|}{3\sigma_r}\right) \tag{13}$$

where σ_t, σ_r are the standard deviations of the Z-axis control errors in E_t and E_r respectively. Based on the confidence level values, the weight coefficients $\gamma_t(p,q)$ and $\gamma_r(p,q)$ defined in (10) can be then calculated as

$$\gamma_t(p,q) = \frac{\eta_t(p,q)\xi(p,q)}{\sum_{(p',q')\in\Omega_2}\eta_t(p',q')\xi(p',q')} \tag{14}$$

$$\gamma_r(p,q) = \frac{\eta_r(p,q)\xi(p,q)}{\sum_{(p',q')\in\Omega_2}\eta_r(p',q')\xi(p',q')} \tag{15}$$

where $\xi(p,q)$ is the following forgetting factor:

$$\xi(p,q) = \frac{1}{\theta_2 + (p-i)^2 + (q-j)^2} \tag{16}$$

with θ_2 being a small positive constant introduced to avoid singularity.

IV. Simulation and Experimental Results

A. Simulations

To verify the validity of the proposed trace and retrace scanning combined topography reconstruction strategy, some simulation tests are first taken in a virtual AFM system [31]. Specifically, the contact mode is chosen to implement the simulation tests, which mainly demonstrate the effect of the combination step. Please note that the full TRSC topography reconstruction strategy, including the hysteresis compensation and alignment steps, will be tested in the subsequent experiments.

The model and parameters of a practical AFM system are adopted to implement the illustrative study. That is, a 3rd order model is utilized to describe the Z-axis dynamics of the piezo-scanner:

$$G(s) = \frac{6.283\times10^4 s^2 + 1.935\times10^7 s + 1.168\times10^{13}}{s^3 + 6.306\times10^4 s^2 + 1.837\times10^8 s + 1.1063\times10^{13}} \tag{17}$$

and the voltage amplifier and position sensor detector sensitivity are chosen as 16 and $9.7\times10^{-9} nm/V$ [15]. For the other parameters, please refer to [31].

Calibration grating is one of the most commonly used testing samples because of its tough surface topography. For the simulation, square samples with height of 12nm, duty ratio of 50% are utilized as the virtual samples, and the obtained results are shown in Fig. 4, with Fig. 4(a) and Fig. 4(b) exhibiting the results under the scanning frequency of 10Hz and 50Hz, respectively.

It can be seen from Fig. 4 that the proposed TRSC combination imaging method provides much better performance than either trace or retrace scanning method. In fact, as shown from Fig. 4(b), when the scanning frequency is set sufficiently high as 50Hz, either the obtained trace or retrace topograph deviates badly from the square form, while the TRSC method still yields a trusty image for the virtual sample. In Fig. 4(b), a little distortion, called as sunken phenomenon, appears in the resulting curve of the TRSC method. This drawback is caused by the control performance degradation for both trace and retrace scanning processes. Similar distortion appears in the subsequent experimental results of Fig. 6(b). Please note that the sunken phenomenon can be mitigated by employing more advanced control methods to improve control performance.

This article has been accepted for publication in a future issue of this journal, but has not been fully edited. Content may change prior to final publication. Citation information: DOI 10.1109/TNANO.2015.2494019, IEEE Transactions on Nanotechnology

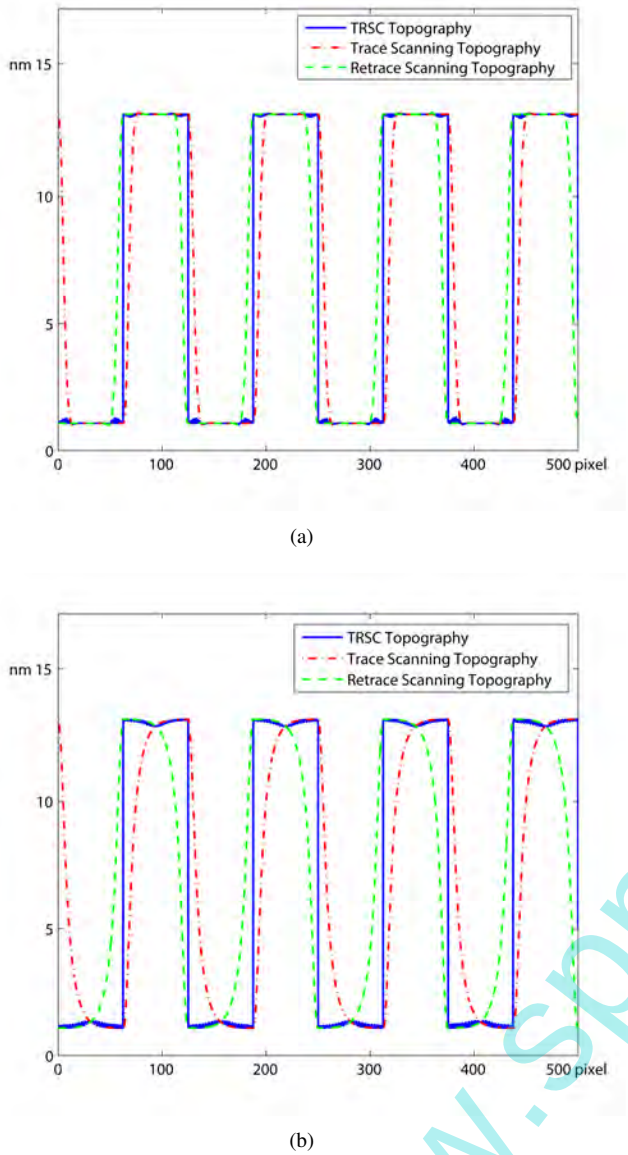

Fig. 4. Calibration grating scanning simulation results: (a) 10Hz scanning results; (b) 50Hz scanning results.

Remark 3: Simulation tests are also taken for general asymmetric samples, with the collected results showing the good performance of the proposed TRSC imaging method, either for slow or fast scanning tasks. Yet, these results are not included into the manuscript due to the space limitation.

B. Experimental results

To further demonstrate the performance of the proposed TRSC topography reconstruction strategy, some experiments are conducted on an AFM system. This system is composed of four parts: a commercial AFM apparatus (CSPM 4000, Being-Nano Inc., P.R. China), high-performance cantilevers (CSC21/Cr-Au, μMasch Inc., USA), a self-developed RT-Linux based real-time control platform [32], and an additional high-quality capacitive displacement sensor (ADE MicroSence 8810). The control period for this system is set as $50\mu s$, equivalent to a wide control bandwidth of 20Khz. Proportional-integral (PI) control strategy is utilized for Z-axis feedback control. The capacitive displacement sensor has a high bandwidth of 10Khz and an accuracy of 0.01nm, which is capable to obtain the hysteresis characters even in fast scanning speed as 50Hz line frequency. The scanning sample is a calibration grating (μMasch Inc., USA) with nominal height of 84nm$\pm$1.5nm and period of $3\mu m$. The experiments are implemented in contact mode.

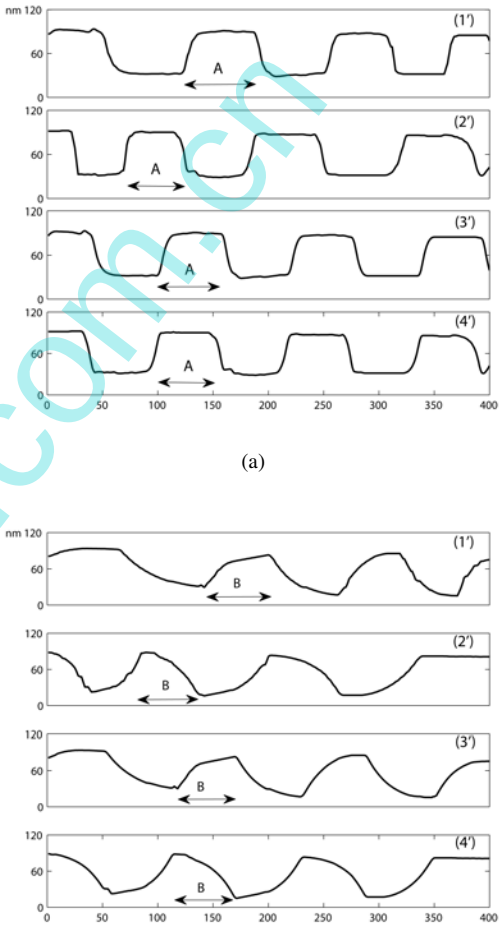

Fig. 5. One-line topography experimental results: (a) 10Hz (b) 50Hz; in both subfigure: (1') and (3') present the trace scanning topography before and after the two steps, hysteresis compensation and alignment, respectively, (2') and (4') present retrace scanning topography before and after the two steps respectively. The segments A, B stand for the same part in either subfigure.

Firstly, the results for the first two steps of hysteresis compensation and alignment will be shown. The sample is scanned at the speed of 10Hz, and 50Hz line frequency, respectively, with the scanning scope set as $10\mu m \times 10\mu m$, and the image resolution as 400×400 pixels. The one-line topography results are shown in Fig. 5.

In Fig. 5(a), the segments A in four subplots show the same part on the sample, however, in (1') and (2'), before the two steps, segment A is obviously not consistent with each other. Meanwhile, in (3') and (4'), the segment A is well aligned

This article has been accepted for publication in a future issue of this journal, but has not been fully edited. Content may change prior to final publication. Citation information: DOI 10.1109/TNANO.2015.2494019, IEEE Transactions on Nanotechnology

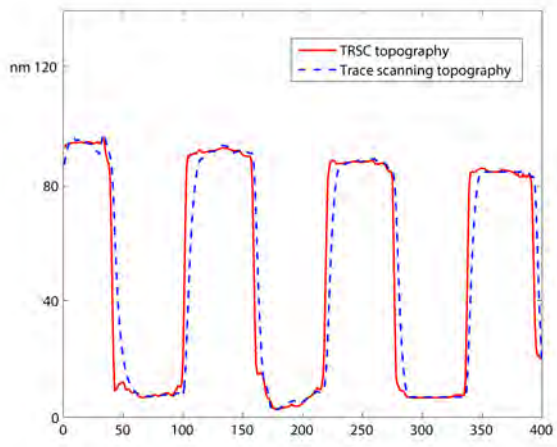

(a)

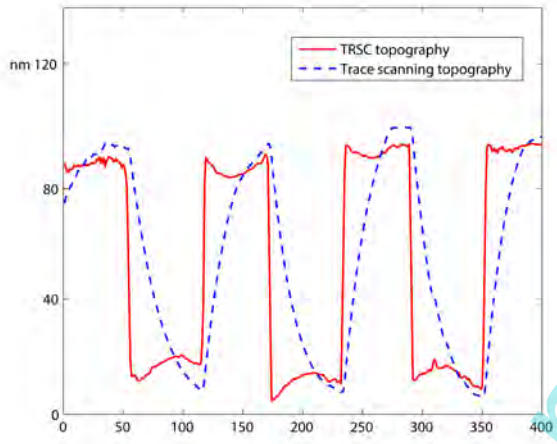

(b)

Fig. 6. Calibration grating scanning results comparison between the TRSC topography and the trace scanning topography:(a) 10Hz, (b) 50Hz.

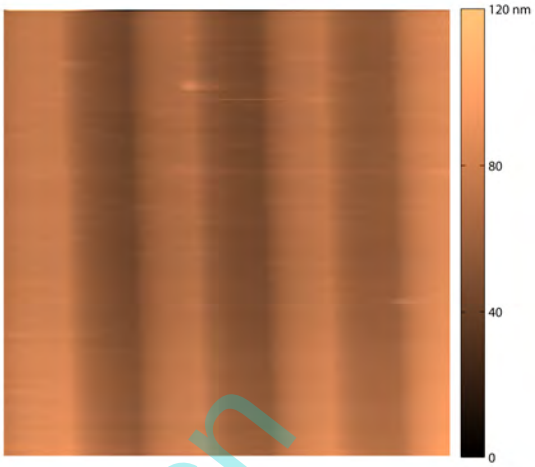

(a) Trace scanning topography

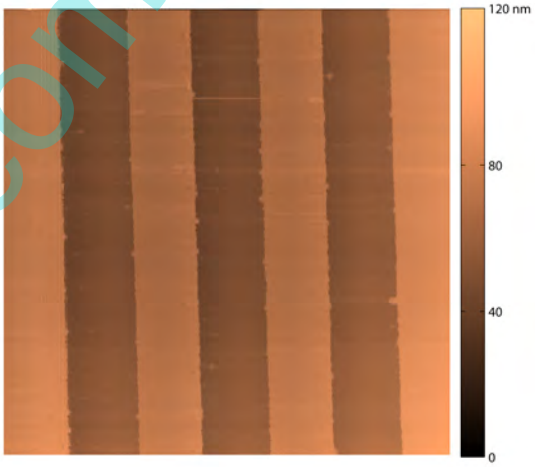

(b) TRSC topography

Fig. 7. Calibration grating topography image comparison for 50Hz line frequency. Scanning scope: $10\mu m \times 10\mu m$, resolution: 400×400 pixels: (a)Trace scanning, (b)TRSC imaging method.

after the designed alignment step. The same situation appears in Fig. 5(b) with segment B. Therefore, after the two steps, the trace topography line is satisfactorily consistent with the retraced line, implying a good foundation for the combination step.

Fig. 6 shows the final one-line results of the proposed TRSC method. The scanning speed is also 10Hz, and 50Hz line frequency, respectively. From the one-line topography, we can see that, at the up-edges and down-edges of the grating, the combined topography line is obviously consistent with the actual calibration grating, much better than the result from the conventional trace method, especially for fast scanning speed shown in Fig. 6(b). In fact, As can be seen from Fig. 6(b), because of the high scanning speed of 50Hz, the original trace and retrace scan lines are both distorted seriously; therefore the combined line shows some distortion as in the midst of the grating steps, which is similar as the result of Fig. 4(b). Delightfully, it still shows much improvement over the traditional trace scanning method.

Fig. 7 shows the comparison between the trace scanning topography image, and the TRSC topography image for 50Hz line frequency, $10\mu m \times 10\mu m$ scanning scope. Because of the slowly ascending character at the grating edges as shown in Fig. 6(b), the trace scanning image Fig. 7(a) is really blurry, while the result obtained by the TRSC method, as shown in Fig. 7(b), is still well consistent with the practical sample. Fig. 8 shows the comparison for the results of 20Hz line frequency with $20\mu m \times 20\mu m$ scanning scope, which further shows the superior performance of the proposed TRSC imaging method.

C. Applications

The proposed TRSC imaging method is applied to scan a biological specimen of E. Coli in air. The E. Coli strain was grown in LB medium at 37 °C with shaking at 150 rpm. Then

This article has been accepted for publication in a future issue of this journal, but has not been fully edited. Content may change prior to final publication. Citation information: DOI 10.1109/TNANO.2015.2494019, IEEE Transactions on Nanotechnology

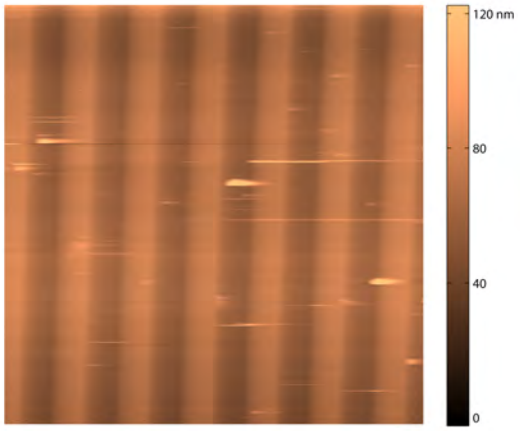

(a) Trace scanning topography

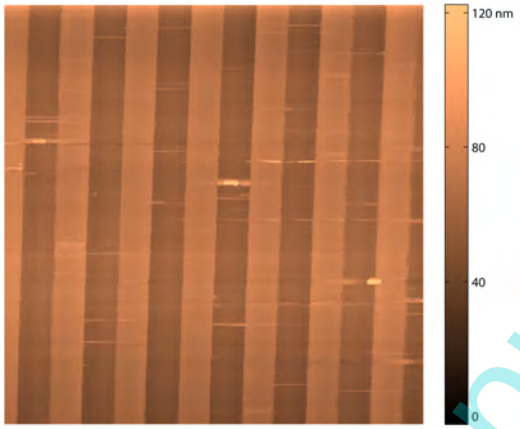

(b) TRSC topography

Fig. 8. Calibration grating topography image comparison for 20Hz line frequency. Scanning scope: $20\mu m \times 20\mu m$, resolution: 400×400 pixels: (a)Trace scanning, (b)TRSC imaging method.

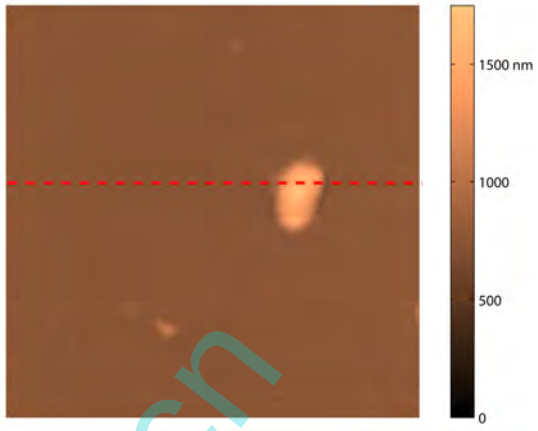

(a) 10Hz TRSC topography results

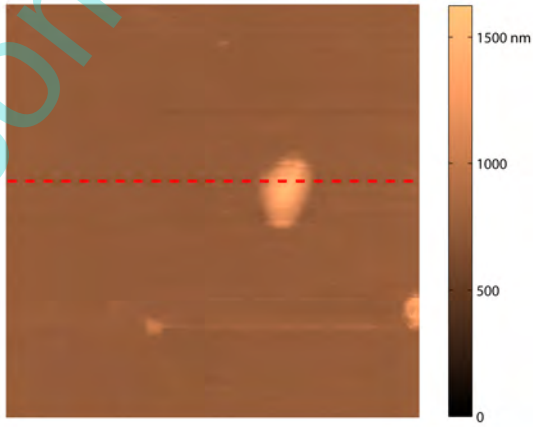

(b) 50Hz TRSC topography results

Fig. 9. Applications for scanning E. Coli specimen in air with TRSC imaging method. The scanning scope is $10\mu m \times 10\mu m$, and the image resolution is 400×400 pixels. (a) 10Hz line frequency, (b) 50Hz line frequency.

it was diluted to a suitable concentration and was added to the surface of newly cleavaged mica. The scanning was performed after drying the mica surface under a nitrogen.

The scanning scope is set as $10\mu m \times 10\mu m$, the image resolution is 400×400 pixels, and the scanning speed is chosen as 10Hz and 50Hz line frequency. From the topography images shown in Fig. 9, it can be seen that even in 50Hz scanning tasks, the obtained image still provides trusty topography for the E. Coli. Furthermore, the section profile comparison is provided in Fig. 10, which is conducted with the 180th row data from Fig. 9, as marked with the red dashed line. It is clearly shown that the raised E. Coli profiles are well consistent with each other, in spite of a little horizontal bias caused by the positioning deviation between 10Hz and 50Hz scanning.

Therefore, the proposed TRSC imaging method gives an evident boost for the imaging accuracy in fast scanning tasks without much information lost.

Remark 4: All the experiments and applications here are implemented in contact mode. In fact, for AC mode, the cantilever dynamics should be considered in (12),(13) to determine the confidence levels. This further study will be conducted in our future work.

V. Conclusion

In this paper, a trace and retrace scanning combined topography reconstruction strategy for an atomic force microscopy is proposed to enhance its imaging performance, especially for fast scanning tasks. Firstly, data fusion based hysteresis compensation is conducted, then a feature point based trace and retrace alignment is implemented; the preceding two steps reach a basis for the following combination task. Subsequently, the trace and retrace scanning topographies are combined together to calculate the final accurate sample surface topography. The efficacy of the proposed imaging method is

This article has been accepted for publication in a future issue of this journal, but has not been fully edited. Content may change prior to final publication. Citation information: DOI 10.1109/TNANO.2015.2494019, IEEE Transactions on Nanotechnology

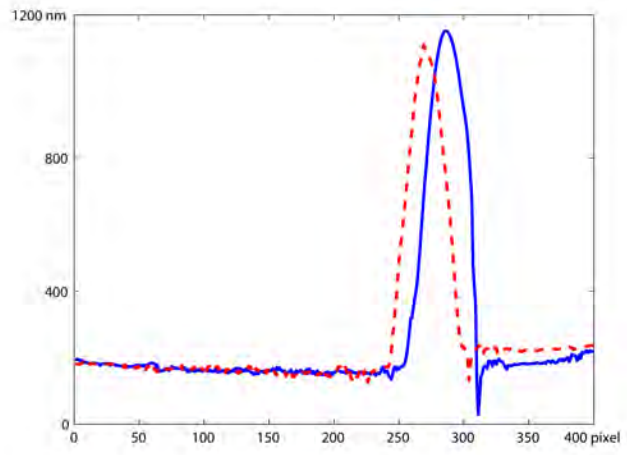

Fig. 10. Section profile comparison for the E. Coli scanning with the 180th row data in Fig. 9. The red dashed line is for 50Hz TRSC imaging, while the blue solid line is for 10Hz TRSC imaging.

verified by the provided simulation and experimental results of scanning calibration gratings at different speeds. It is shown that this imaging method has markedly enhanced the imaging performance, particularly for fast scanning tasks.

Our future work will apply the proposed TRSC method to scan certain biological samples with sufficiently high speed, so as to enable biologists to study their dynamic properties. It will not be restricted to atmosphere environment, the scanning tasks in liquid will be tried too. We will also focus on designing some more advanced combination strategies and some more efficient non-raster scan patterns to obtain satisfactory images when scanning at even higher speed.

VI. Acknowledgements

Thanks to Dr. Ming Wu, and Pro. Xizeng Feng from College of Life Science, Nankai University, Tianjin, China, for the professional works of preparing the E. Coli samples.

References

[1] G. K. Binnig, C. F. Quate, and C. Gerber, Atomic force microscope, *Physical Review Letters*, vol. 56, pp. 930-933, March 3, 1986.

[2] T. Ando, High-speed atomic force microscopy coming of age, *Nanotechnology*, vol. 23, no. 6, p. 062001, 2012.

[3] G. Mangamma, S. Dash, and A. K. Tyagi, AFM investigations on N+ implanted TiN, *IEEE Transactions on Nanotechnology*, vol. 12, no. 6, pp. 1007-1011, 2013.

[4] S. A. L. Weber, J. I. Kilpatrick, T. M. Brosnan, S. P. Jarvis, and B. J. Rodriguez, High viscosity environments: an unexpected route to obtain true atomic resolution with atomic force microscopy, *Nanotechnology*, vol. 25, no. 17, p. 175701, 2014.

[5] Y. Peng, Z. Wang, and C. Li, Study of nanotribological properties of multilayer graphene by calibrated atomic force microscopy, *Nanotechnology*, vol. 25, no. 30, p. 305701, 2014.

[6] A. J. Fleming, Dual-stage vertical feedback for high-speed scanning probe microscopy, *IEEE Transactions on Control Systems Technology*, vol. 19, no. 1, pp. 156-165, 2010.

[7] Y. Seo, C. S. Choi, S. H. Han, and S. J. Han, Real-time atomic force microscopy using mechanical resonator type scanner, *Review of Scientific Instruments*, vol. 79, no. 10, p. 103703(2008).

[8] B. J. Kenton and K. K. Leang, Design and control of a three-axis serial-kinematic high-bandwidth nanopositioner, *IEEE/ASME Transactions on Mechatronics*, vol. 17, no. 2, pp. 356-369, April 2012.

[9] N. Xi, B. Song, R. Yang, K. W. C. Lai, H. Chen, Video rate atomic force microscopy: use of compressive scanning for nanoscale video imaging, *Nanotechnology Magazine*, IEEE, vol. 7, no. 1, pp. 4-8, 2013.

[10] S. Kuipera, G. Schitter, Model-based feedback controller design for dual actuated atomic force microscopy, *Mechatronics*, vol. 22, no. 3, pp. 327-337, 2012.

[11] Y. K. Yong, B. Bhikkaji,S. O. R. Moheimani, Design, modeling, and FPAA-based control of a high-speed atomic force microscope nanopositioner, *IEEE/ASME TRANSACTIONS ON MECHATRONICS*, vol. 18, no. 3, pp. 1060-1071, 2013.

[12] Y. K. Yong, S. O. R. Mohemani, Design of an inertially counterbalanced Z-nanopositioner for high-speed atomic force microscopy, *IEEE Transactions on Nanotechnology*, vo. 12. no. 2, pp. 137-145, 2013.

[13] Y. Fang, Y. Zhang, N. Qi, and X. Dong, AM-AFM systems analysis and output feedback control design with sensor saturation, *IEEE Transactions on Nanotechnology*, vo. 12. no. 2, pp. 190-202, 2013.

[14] M. S. Rana, H. R. Pota, and I. R. Petersen, High-speed AFM image scanning using observer-based MPC-notch control, *IEEE Transactions on Nanotechnology*, vol. 12, no. 2, pp. 246-254, 2013.

[15] X. Ren, Y. Fang, N. Qi, M. Wu, X. Feng, A practical dynamic imaging method for fast scanning AFMs, *Instrumentation Science and Technology*, vol. 41, iss. 4, pp. 394-405, July 2013.

[16] Y. Zhang, Y. Fang, J. Yu, and X. Dong, Note: A novel atomic force microscope fast imaging approach: variable-speed scanning, *Review of Scientific Instruments*, vol. 82, no. 5, p. 056103(2011).

[17] I. A. Mahmood, S. O. R. Moheimani, and B. Bhikkaji, A new scanning method for fast atomic force microscopy, *IEEE Transactions on Nanotechnology*, vol. 10, no. 2, pp. 203-216, March 2011.

[18] D. Ebeling and H. Holscher, Analysis of the constant-excitation mode in frequency-modulation atomic force microscopy with active Q-control applied in ambient conditions and liquids, *Journal of Applied Physics*, vol. 102, no. 11, p. 114310, 2007.

[19] S. Kuiper, P. Van den Hof, and G. Schitter, Towards integrated design of a robust feedback controller and topography estimator for atomic force microscopy, *in Proceedings of the 18th IFAC World Congress*, Milan, Italy, 2011, pp. 12709-12714.

[20] T. Tuma, J. Lygeros, V. Kartik, A. Sebastian, A. Pantazi, High-speed multiresolution scanning probe microscopy based on lissajous scan trajectories, *Nanotechnology*, vol. 23, no. 18, p. 185501, 2012.

[21] J. Ren, and Q. Zou, High-speed adaptive contact-mode atomic force microscopy imaging with near-minimum-force, *Review of Scientific Instruments*, 2014, 85(7): 073706.

[22] N. Qi, Y. Fang, X. Ren, and Y. Wu, Varying-gain modeling and advanced DMPC control of an AFM system, *IEEE Transactions on Nanotechnology*, vol. 14, no. 1, pp. 82-92, 2015.

[23] B. Bhikkaji, Y. K. Yong, I. A. Mahmood, S. O. R. Moheimani. Diagonal control design for atomic force microscope piezoelectric tube nanopositioners, *Review of Scientific Instruments*, 2013, 84(2): 023705.

[24] S. Salapaka, A. Cleveland, et al. High bandwidth nano-positioner: a robust control approach, *Review of Scientific Instruments*, 2002, 73(9): 3232-3241.

[25] Y. Zhang, Y. Fang, X. Dong, X. Zhou. A novel learning control strategy for hysteresis and vibration of piezo-scanners, *in Proceedings of the 48th IEEE Conference of Decision and Control, and the 28th Chinese Control Conference*, 2009, Shanghai, P.R. China, Dec. 16-18,2009, pp. 750-755.

[26] Y. Wu, Q. Zou, Robust Inversion-based 2-DOF control design for output tracking: piezoelectric-actuator example, *IEEE Transactions on Control Systems Technology*, 2009, 17(5), pp. 1069-1082.

[27] K. S. Kim, and Q. Zou, A model-free inversion-based iterative feedforward control for precision output tracking of linear time-invariant systems, *IEEE/ASME Transactions on Mechatronics*, 2013, vol. 18, no. 6, pp. 1767-1777.

[28] X. Zhao, Y. Tan. Modeling hysteresis and its inverse model using neural networks based on expanded input space method, *IEEE Transactions on Control Systems Technology*, 2008, 16(3): 484-490.

[29] A. Hatch, R. Smith, et al. Construction and experimental implementation of a model-based inverse filter to attenuate hysteresis in ferroelectric transducers, *IEEE Transactions on Control Systems Technology*, 2006, 14(6): 1058-1069.

[30] Y. Zhang, Y. Fang, X. Zhou, et al. Image-based hysteresis modeling and compensation for an AFM piezo-scanner, *Asian Journal of Control*, 2009, 11(2): 166-174.

[31] X. Zhou, Y. Fang, A virtual tapping-mode atomic force microscope, *in Proceedings of the 1st IEEE International Conference of Nano/Micro Engineered and Molecular Systems*, pp. 501-504, Zhuhai, China, January 2006.

[32] X. Zhou, Y. Fang, X. Dong, Y. Zhang, Real-time feedback control system for AFM based on RTLinux, *Computer Engineering*, 34(15): 226-228, 2008.

Xiao Ren received the B.S. degree in automation from Tianjin University, Tianjin, China, in 2011. He is currently working toward the Ph.D. degree in the Institute of Robotics and Automatic Information System, Nankai University, Tianjin.

His research interests include nanomanipulation, fast scanning atomic force microscopies, and nonlinear characters for piezo-scanners.

Yongchun Fang (S'00−M'02−SM'08) received the B.S. degree in electrical engineering and the M.S. degree in control theory and applications from Zhejiang University, Hangzhou, China, in 1996 and 1999, respectively, and the Ph.D. degree in electrical engineering from Clemson University, Clemson, SC, in 2002.

From 2002 to 2003, he was a Postdoctoral Fellow with the Sibley School of Mechanical and Aerospace Engineering, Cornell University, Ithaca, NY. He is currently a Professor with the Institute of Robotics and Automatic Information System (IRAIS), Nankai University, Tianjin, China. His research interests include AFM-based Nano-systems, visual servoing, and control of underactuated systems including overhead cranes.

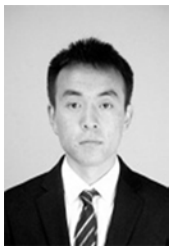

Yinan Wu received the B.S. degree in automation from Nankai University, Tianjin, China, in 2013. He is currently working toward the Ph.D. degree in the Institute of Robotics and Automatic Information System, Nankai University, Tianjin.

His research interests include compressive sensing ,nanomanipulation and nanopositioning of atomic force microscopes.